Scientia Iranica, Vol. 13, No. 4, pp 364 372

SCIENTIA IRANICA

Research Note

A New Analytical Method on the Field Calculation of Interior Permanent-Magnet Synchronous Motors

A. Kiyoumarsi*, M.R. Hassanzadeh[1] and M. Moallem[2]

Although there are analytical methods for field calculation in surface-mounted synchronous motors, accurate analytical methods for predicting airgap flux density distribution in Interior-type Permanent-Magnet (IPM) synchronous motors are not available. In this paper, a novel method for analytical prediction of flux distribution, based on Schwarz-Christofell transformation techniques, is proposed to evaluate the airgap flux density distribution in an IPM motor. To validate the accuracy of the new analytical method, the results are compared with transient Finite Element Method (FEM) results.

INTRODUCTION

An Interior Permanent-Magnet (IPM) synchronous motor has many advantages over other permanent-magnet synchronous motors. It usually has a larger quadrature rather than a direct axis magnetizing reactance. This unequal inductance in different axes enables the motor to have both the properties of a Surface-mounted Permanent-Magnet Synchronous Motor (SPMSM) and a Synchronous Reluctance motor (SynchRel) [1-4].

In an IPM synchronous motor, the effective airgap length on the d-axis is large, so the variation of the d-axis magnetizing inductance, Lmd, due to magnetic saturation, is minimal. For the q-axis, there is an inverse condition, i.e., the effective airgap length on the q-axis is small and, therefore, the saturation effects are significant [4]. In this paper, an analytical method for the prediction of the flux density distribution is proposed and results are also compared with those obtained from a finite element method analysis.

The following section introduces a brief comparison between different mappings that can be used for the transformation of the motor topology to a new plane and, then, after selection of one of them, this conformal mapping is used for calculating the new boundaries of the rotor core and stator inner surface. After that, the application of transient finite element analysis for the magnetic field calculation of an IPM synchronous motor is presented and, also, motor-drive operation is discussed. The results of the new analytical method and, also, the numerical method, i.e., transient finite element method, are then compared and, finally, a conclusion is included.

GENERAL ANALYTICAL METHOD

Using Zhu's and Boules' method [5,6], the flux density distribution in the airgap/magnet region can be analytically predicted for Surface-mounted Permanent-Magnet Synchronous (SPMS) motors. Open-circuit and load condition field distributions for the IPM motors can be expressed according to the product of magnet and armature winding flux density distributions and corresponding relative permeance functions [7]. The new relative permeance function of the proposed method can be defined as follows [7]:

$$\tilde{\lambda}(\varphi, r) = \tilde{\lambda}_{\text{STATOR-SLOT}} * \tilde{\lambda}_{\text{ROTOR-SALIENCY}}. \qquad (1)$$

The influence of stator slots in the magnetic field distribution and saliency of the airgap can be considered by $\tilde{\lambda}_{\text{STATOR-SLOT}}$ and $\tilde{\lambda}_{\text{ROTOR-SALIENCY}}$. Figure 1

*. *Corresponding Author, Department of Electronics Engineering, Isfahan University, Isfahan, I.R. Iran.*

1. *Department of Electrical Engineering, Abhar Islamic Azad University, Abhar, Ghazvin, I.R. Iran.*
2. *Department of Electronical and Computer Engineering, Isfahan University of Technology, Isfahan, I.R. Iran.*

shows, approximately, the effect of rotor saliency and its equivalent airgap geometric function.

The normalized airgap permeance function has a Fourier series representation. If the effect of curvature of the rotor is considered, it is required to determine the relative airgap permeance function more accurately. In this paper, conformal mapping is employed to map the cylindrical rotor to a square, so that the airgap length can be determined accurately. At first, a composition of two mappings is presented and, following that, a simplified conformal mapping, by which the transformation is accomplished, is described.

The mapping, which transforms the open disk, ($|w|\langle 1.0$), onto the upper half plane (Figure 2), can be defined as:

$$W = j\frac{1+Z}{1 \quad Z}. \tag{2}$$

The mapping that transforms the upper half plane to a rectangle is given by the Schwarz-Christofell transformation [8,9]:

$$T = \int_0^W \frac{d\eta}{\sqrt{(1 \quad \eta^2)(1 \quad k^2\eta^2)}}, \qquad 0 < k < 1. \tag{3}$$

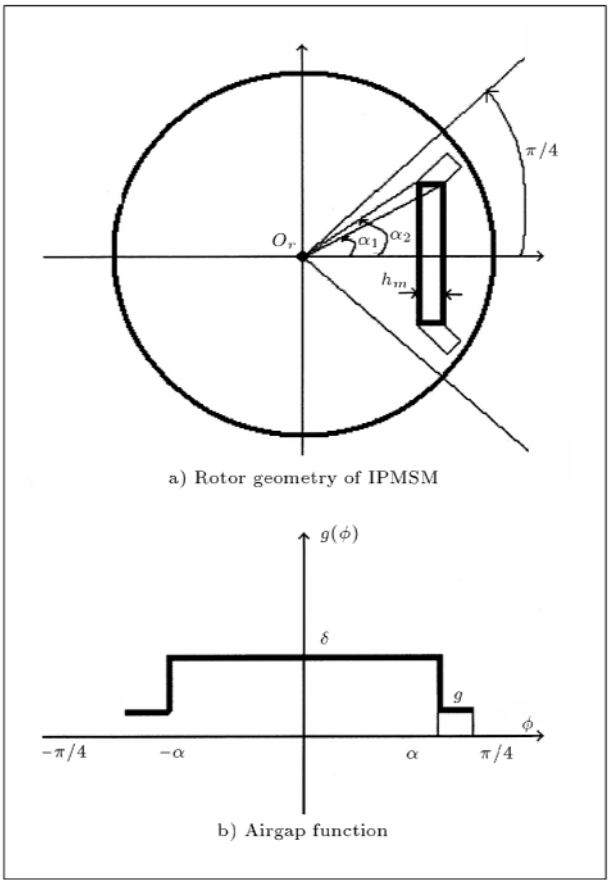

Figure 1. Approximate airgap function.

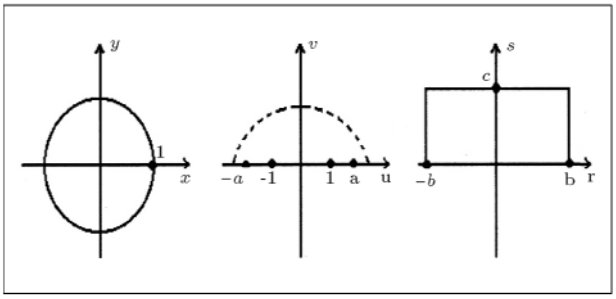

Figure 2. z- w- and t-planes in the conformal transformations.

Composition of the two above mappings is equal to:

$$t = ToW(x,y) = \int_0^{u(x,y)+jv(x,y)} \frac{d\eta}{\sqrt{(1 \quad \eta^2)(1 \quad k^2\eta^2)}}. \tag{4}$$

If the position of a permanent-magnet edge in the rotor is given by curve C, the transformation maps curve C onto curve C', so that;

$$C \begin{cases} x = \gamma_m \\ \gamma_m \tan(\alpha) < y < +\gamma_m \tan(\alpha) \end{cases}, \tag{5}$$

$$C' \begin{cases} u(y) = \frac{2y}{y^2+(1 \quad \gamma_m)^2} \\ v(y) = \frac{(1 \quad \gamma_m)^2 \quad y^2}{y^2+(1 \quad \gamma_m)^2} \\ \gamma_m \tan(\alpha) < y < +\gamma_m \tan(\alpha) \end{cases}. \tag{6}$$

It is usually difficult to calculate the above related elliptic integrals. So, it is better to consider another analytic function that satisfies the Cauchy-Riemann equation, i.e.:

$$f(z) = \log(z) = \ln|z| + j\arg(z). \tag{7}$$

The function, $\log(z)$, is not only continuous in domain D, but also, analytic in that domain, with the property:

$$\frac{d}{dz}\log(z) = \frac{1}{z} \neq 0, \tag{8}$$

where:

$$D = \{z| : |z| > 0, \quad \pi < \arg(z) < \pi\}. \tag{9}$$

The transformation defined in Equation 7 is also a conformal mapping on D (see Appendix 1). The image of any point (x,y) in the z-plane is the point (u,v) in the w-plane, whose rectangular coordinates are defined, representatively, as follows:

$$u(x,y) = \frac{1}{2}\ln(x^2+y^2),$$

$$v(x,y) = \arctan(y/x). \tag{10}$$

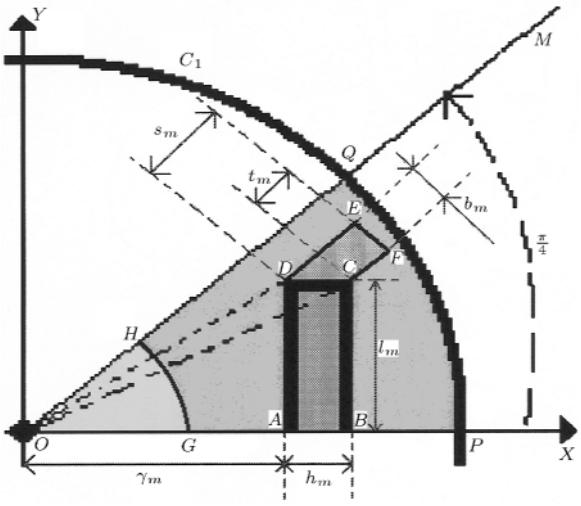

Figure 3. Cross section of the rotor of interior PM synchronous motor.

According to Figure 3, the first octave of circle C_1 is transformed into line L_1, with the parametric representation written in the following equation:

$$C_1 \begin{cases} x = R_{ri}\cos(\theta) \\ y = R_{ri}\sin(\theta) \end{cases}, \qquad 0 < \theta < \pi/4, \tag{11}$$

$$L_1 \begin{cases} u(x,y) = \ln(R_{ri}) \\ v(x,y) = \theta \end{cases}, \qquad 0.0 < \theta < \frac{\pi}{4}. \tag{12}$$

Also, segment line $AD(C_2)$ is transformed into curve L_2, with the following parametric representations:

$$C_2 \begin{cases} x = \gamma_m \\ y = \gamma_m \tan(\theta) \end{cases}, \qquad 0 < \theta < \pi/4, \tag{13}$$

$$L_2 \begin{cases} u(x,y) = \ln\left(\frac{\gamma_m}{\cos(v)}\right) \\ 0 \le v(x,y) \le +\alpha_2 \end{cases}. \tag{14}$$

Here, angle α_2 is defined as angle $\angle AOD$. In addition, segment line $BC(C_3)$ is transformed into curve L_3, with the following parametric representations:

$$C_3 \begin{cases} x = \gamma_m + h_m \\ y = (\gamma_m + h_m)\tan(\theta) \end{cases}, \qquad 0 < \theta < \pi/4, \tag{15}$$

$$L_3 \begin{cases} u(x,y) = \ln\left(\frac{\gamma_m + h_m}{\cos(v)}\right) \\ 0 \le v(x,y) \le +\alpha_1 \end{cases}. \tag{16}$$

Here, angle α_1 is defined as angle $\angle BOC$.

The segment line, $DC(C_4)$, is transformed into curve L_4, with the following parametric representations:

$$C_4 \begin{cases} x = l_m/\tan(\theta) \\ y = l_m \end{cases}, \qquad \alpha_1 \le \theta \le \alpha_2, \tag{17}$$

$$L_4 \begin{cases} u(x,y) = \ln\left(\frac{l_m}{\sin(v)}\right) \\ \alpha_1 \le v(x,y) \le \alpha_2 \end{cases}. \tag{18}$$

Following the above procedure for obtaining the transformed curves for the original lines and curves, the mapping of segment lines DE, EF and FC, as the domain of definition for the transformation, can be extended.

For the machine with parameters as shown in Appendix 2 and using the above mentioned mapping, the image of the transformed domains, whose boundaries involve segment lines, half lines and curves, is shown in Figure 4. For every interval on the v-axis, the total airgap length for flux lines in the direction of the u-axis is defined as:

$$\begin{cases} \widetilde{G}(u,v) = \ln\left(\frac{\gamma_m + h_m}{\gamma_m}\right) \\ 0 \le v \le \alpha_1 \end{cases}, \tag{19}$$

$$\begin{cases} \widetilde{G}(u,v) = u_4(v) \quad \ln\left(\frac{\gamma_m}{\cos(v)}\right) \\ \alpha_1 \le v \le \alpha_3 \end{cases}, \tag{20}$$

$$\begin{cases} \widetilde{G}(u,v) = u_5(v) \quad \ln\left(\frac{\gamma_m}{\cos(v)}\right) \\ \alpha_3 \le v \le \alpha_2 \end{cases}, \tag{21}$$

$$\begin{cases} \widetilde{G}(u,v) = u_5(v) \quad u_6(v) \\ \alpha_2 \le v \le \alpha_4 \end{cases}, \tag{22}$$

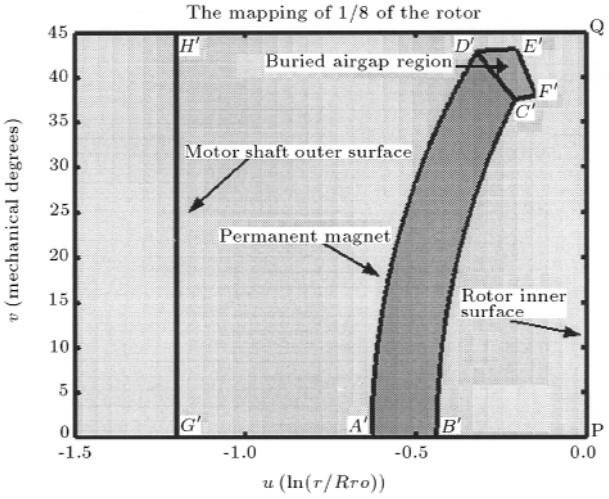

Figure 4. Mapping of the cross section of rotor of an interior PM synchronous motor.

where functions $u_4(.)$, $u_5(.)$ and $u_6(.)$ are obtained by mapping the relations of segment lines CF, FE and ED. α_3 and α_4 can be defined in points F and E, respectively, by the following relations:

$$v \text{ at point F} \equiv \alpha_3,$$

$$v \text{ at point E} \equiv \alpha_4. \tag{23}$$

Consequently, according to the above curve representations for different inner rotor topologies, the airgap function can now be given as:

$$\delta(v) = g_0 + R_{ri}\left(\exp\left(\widetilde{G}_i(v)\right) \quad \exp\left(\widetilde{G}_j(v)\right)\right). \tag{24}$$

So, the new relative permeance function of the airgap that includes the effect of rotor saliency is, approximately, equal to:

$$\widetilde{\lambda}_{\text{ROTOR-SALIENCY}}(\theta, r)\Big|_{r=rg} = \frac{\delta_0}{\delta(\theta)}. \tag{25}$$

In the above formula,

$$\delta_0 = g_0 + \frac{h_m}{\mu_r}. \tag{26}$$

Now, the transformed airgap function is shown in Figure 5.

The influence of stator slots on the magnetic field distribution in the airgap region can be successfully modeled using the following relative permeance function [10]:

$$\widetilde{\lambda}_{\text{SLOT}}(\theta, r)\Big|_{r=r_g} = \sum_{n=0}^{\infty} \widetilde{\Lambda}_n(r_g)\cos(nQ_s[\theta + \alpha_{sa}]). \tag{27}$$

The airgap flux density distribution obtained by these relative permeance functions can now be evaluated using:

$$B_{\text{open-circuit}}(r, \alpha, t) = B_{\text{magnet}}(r, \alpha, t)\widetilde{\lambda}(r, \alpha). \tag{28}$$

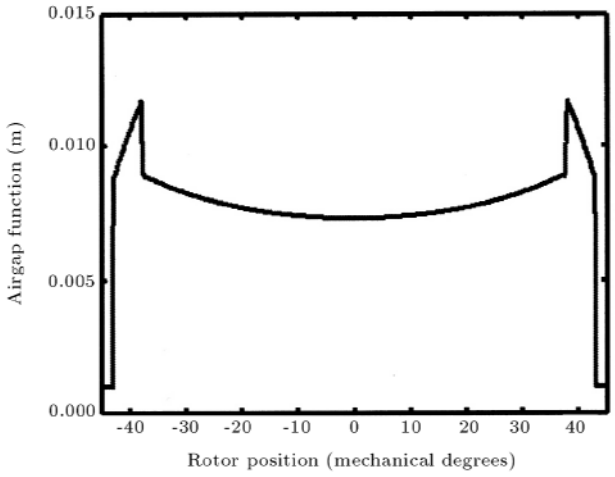

Figure 5. Modified airgap function profile.

SIMULATION RESULTS

For validation of the new proposed method, a fully-pitched, double-layer winding interior-type PM synchronous motor drive is considered. The motor is a 5HP, 1500rpm, 4-pole synchronous motor. Figure 6 shows flux lines at a rotor position, on the basis of a time-stepped transient finite elements analysis of the motor. The rotor and stator are of ferromagnetic materials, i.e. M-19 and M-36, respectively and the field excitation consists of four PMs of the Nd-Fe-B(N33) type. A Lagrangian sliding interface path (surface) is also used to consider the effect of rotor mesh movement in a torque calculation process. The analysis is based on the transient electromagnetic finite element formulation with rotor motion (flowchart of Figure 7). The airgap of the machine is divided into two layers. This two-layer airgap region is used and constraint equations are enforced between these two

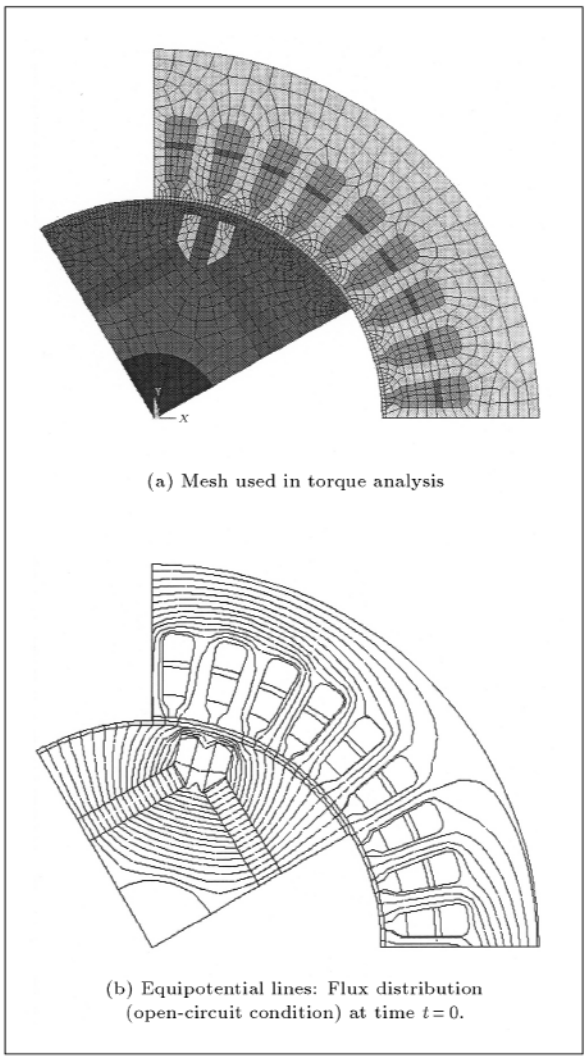

Figure 6. A mesh used in torque analysis and flux lines at a rotor position.

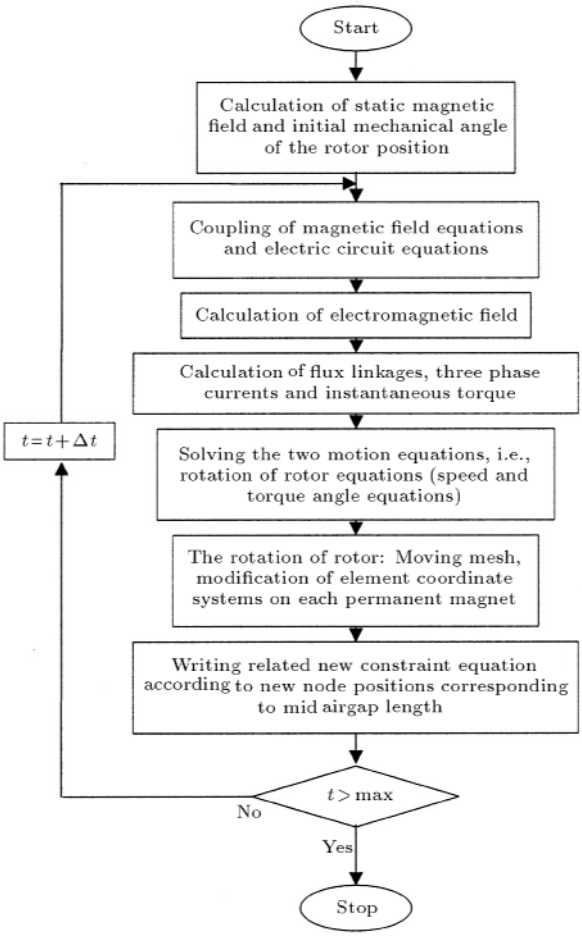

Figure 7. Transient finite element method.

layers. The fundamental component of the flux density distribution, obtained by transient finite element analysis, at time zero, is:

$$B_{\text{open-circuit}}(\theta \quad \theta_r) = 0.6485\cos(2[\theta \quad \theta_r]). \tag{29}$$

And the one obtained by the new analytical method, without considering the buried airgap region, is, as follows:

$$B_{\text{open-circuit}}(\theta \quad \theta_r) = 0.5717\cos(2[\theta \quad \theta_r]). \tag{30}$$

Also, the one obtained by the new analytical method, considering the barrier (buried airgap) region, is:

$$B_{\text{open-circuit}}(\theta \quad \theta_r) = 0.5456\cos(2[\theta \quad \theta_r]). \tag{31}$$

Figures 8 to 18 show the flux density distribution in the mid-airgap region and back-EMF, obtained by FEM and analytical techniques. Figures 8 and 9 show flux density distribution and its spectrum obtained by FEM results. Figures 10 and 11 also show Back-EMF and its spectrum obtained by FEM results. In addition, Figures 12 and 13 show the flux density distribution and its spectrum obtained by the new analytical method. Figures 14 and 15 show Back-EMF and its spectrum

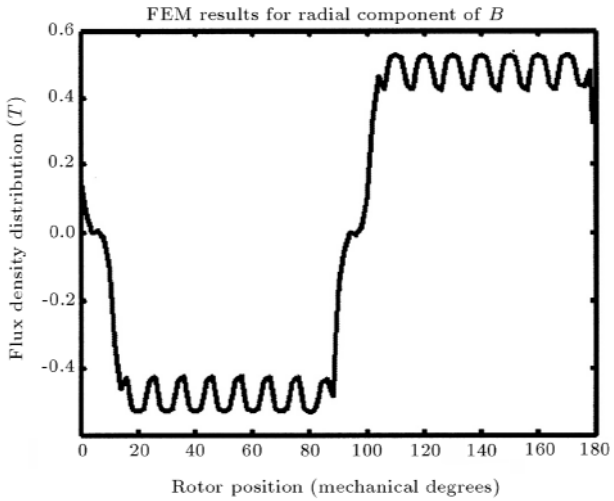

Figure 8. Flux density distribution. FEM results for radial componanat of 8.

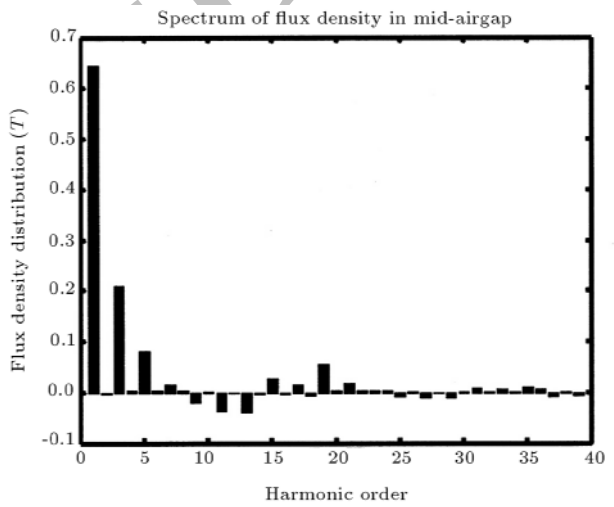

Figure 9. Flux density distribution (FEM results). Spectrum of flux density in mid-airgap.

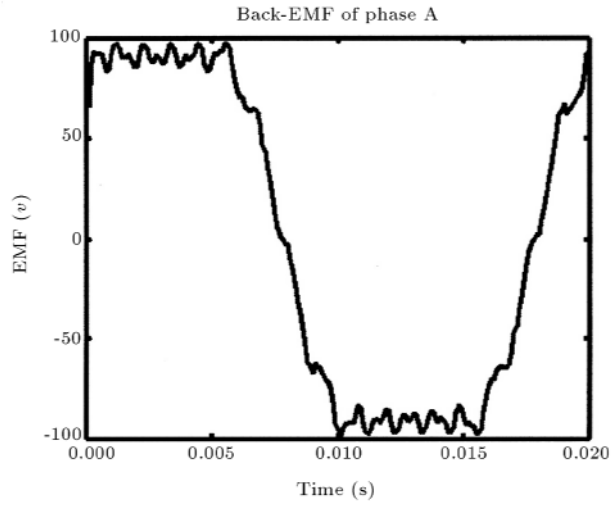

Figure 10. Back-EMF (FEM results) of phase A.

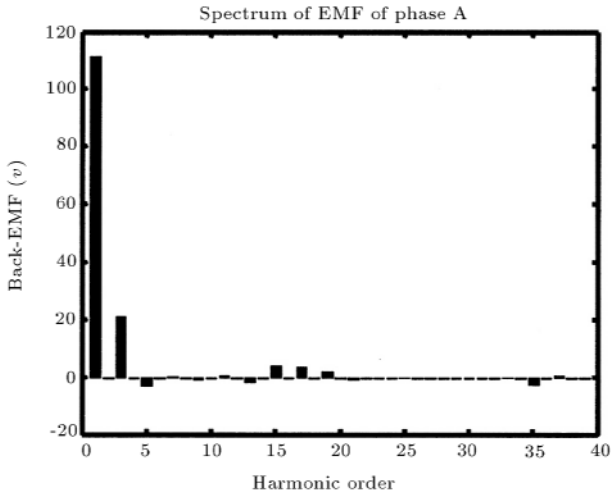

Figure 11. Back-EMF (FEM results); spectrum of EMF of phase A.

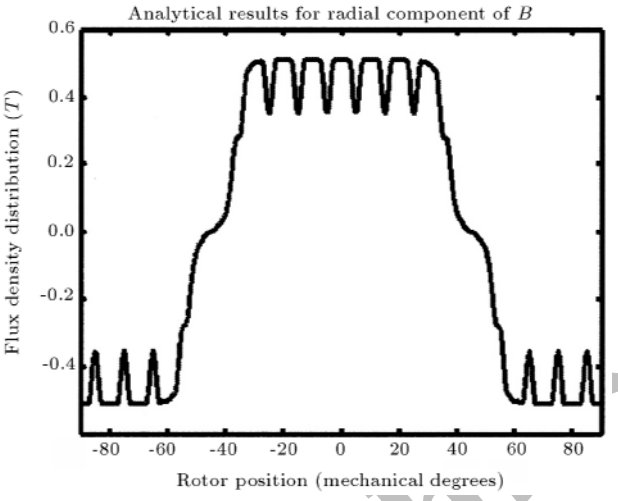

Figure 12. Flux density distribution; analytical results for radial componant of B.

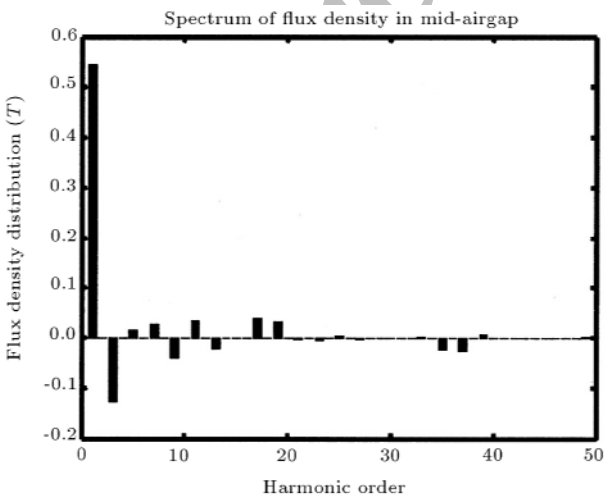

Figure 13. Flux density distribution (analytical results); spectrum of flux density im mid-airgap.

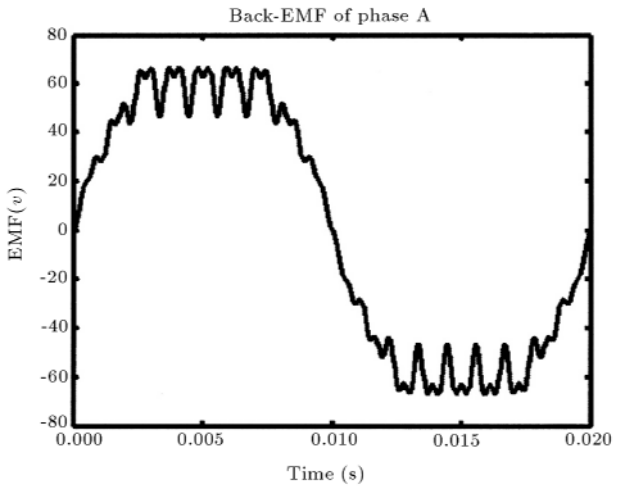

Figure 14. Back-EMF (analytical results) of phase A.

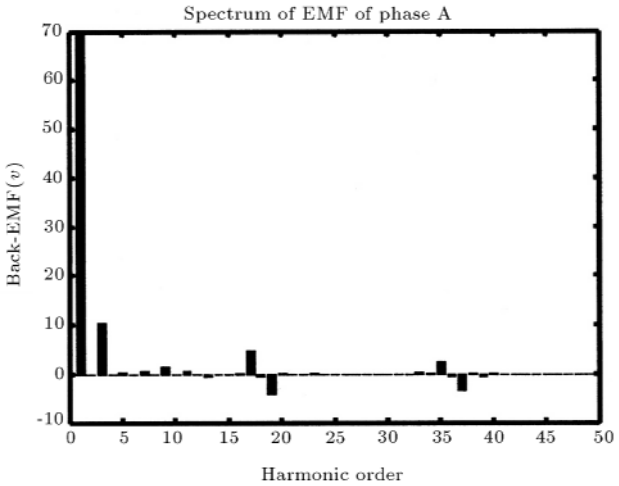

Figure 15. Back-EMF (analytical results); spectrum of EMF of phase A.

obtained by the new analytical method. Figure 16 compares the flux density distribution obtained by FEM results at the mid-airgap region for both radial and tangential components. The spectrum comparison of the results of the FEM and analytical method for flux density distribution at the mid-airgap region are included in Figure 17. Figure 18 also shows the spectrum of the tangential component of flux density distribution at the mid-airgap region obtained by FEM results. By careful consideration of these figures, it is clear that there is an error of about 20 percent between the results of the FEM and the analytical methods; however, the calculation time for FEM is much greater than that of the new analytical technique.

For simplicity, one quarter of the machine has been modeled by FEM and required periodic boundary conditions are also considered as sets of constraint equations between nodes and elements. The analytical back-EMF calculation is calculated using the method

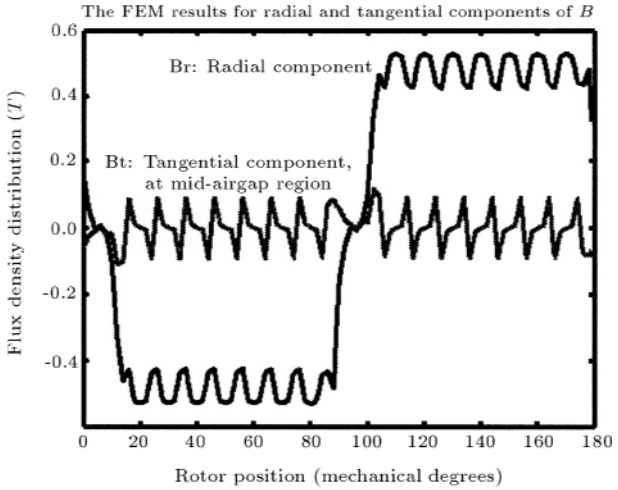

Figure 16. Flux density distribution (FEM results).

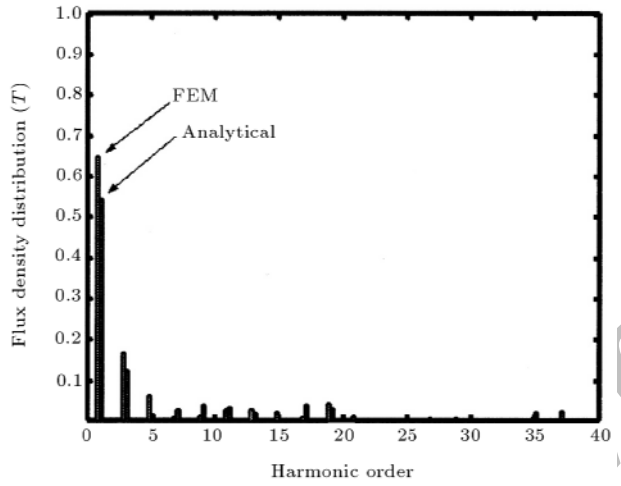

Figure 17. Comparison of flux density distribution at mid-airgap region (radial component) for FEM results and analytical results.

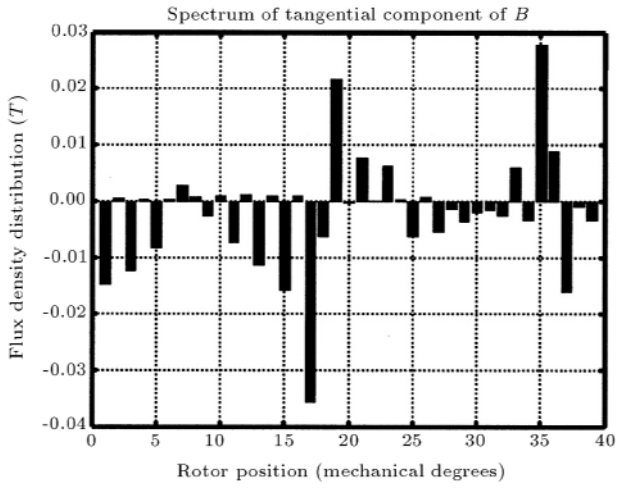

Figure 18. Flux density distribution (FEM results). Tangential component at mid-airgap region.

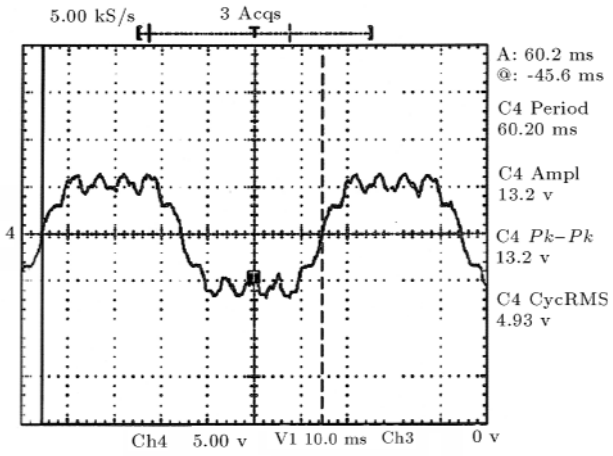

Figure 19. Measured back-EMF [7].

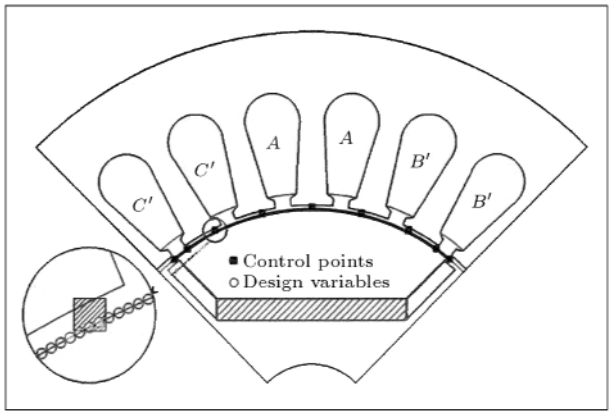

Figure 20. Design model of IPM motor [7].

stated in Appendix 3. On the other hand, in the FEM calculations, at first, the total flux-linkage of phase A is calculated instantaneously in one half period of a rotor revolution, as in the following equation and, then, the back-EMF is determined:

$$\lambda = \frac{N_S}{S} l_r \int Ads. \tag{32}$$

Figure 19 shows the measured back-EMF waveform of a different IPM synchronous motor (Figure 20), with different stator-slot topology; when the rotor was driven under no-load by an external prime mover at a constant speed of 500 rpm. This IPM motor is developed and measured experimentally by Lee et al. [11]. Considering Figures 10, 14 and 19, the validity of the calculations of the analytical method can be seen.

CONCLUSION

The improved relative permanence model for the calculation of space and time harmonics in load and no-load flux density distributions in the airgap of an interior-type permanent-magnet synchronous motor has been

proposed and validation of the analytical method is carried out by the conventional transient finite element method. The effect of stator slots, rotor saliency and magnet shapes can be considered in this model. Thus, this method can be used for those processes with intensive iterative calculations, such as shape and design optimization processes.

NOMENCLATURE

B_{magnet}	flux density due to magnet at stator inside surface
$B_{\text{open-circuit}}$	open-circuit flux density distribution
b_0	stator slot-opening
e_{fA}	back-EMF of phase A
p	number of pole pairs
Q_s	stator slot number
r_g	mid-airgap radius
w_S	equivalent stator slot-opening
w_t	stator tooth width
α	angular displacement between the stator mmf and rotor mmf
α_{sa}	angular displacement between the stator slot axis and the axis of the coils of phase A
$\tilde{\lambda}$	relative permeance function
λ_{PM}	flux linkage due to the permanent magnets
Λ_{ref}	reference permeance

REFERENCES

1. Skvarenina, T.L., *The Power Electronics Handbook*, Purdue University, West Lafayette, Indiana, CRC Press (2002).
2. Meier, S., *Theoretical Design of Surface-Mounted Permanent-Magnet Motors with Field-Weakening Capability*, Master Thesis, Royal Institute of Technology, Stockholm, Sweden (2002).
3. Jahns, T.M. and Soong, W.L. "Interior permanent-magnet synchronous motors for adjustable-speed drives", *IEEE Transactions on Industry Applications*, **IA-22**(4), pp 738-747 (July/Aug. 1986).
4. Boldea, I., *Reluctance Synchronous Machines & Drives*, Oxford University Press (1996).
5. Zhu, Z.Q., Howe, D. and Chan, C.C. "Improved analytical model for predicting the magnetic field distribution in brushless permanent-magnet machines", *IEEE Transactions on Magnetics*, **38**(8), pp 1500-1506 (July 2002).
6. Boules, N. "Prediction of no-load flux density distribution in permanent magnet machines", *IEEE Transactions on Industry Applications*, **IA-21**, pp 633-643 (1985).
7. Boldea, I. and Nasar, S., *The Induction Machine Handbook*, chapters 12-14, CRC Press (2002).
8. Churchill, R.V., Brown, J.W. and Verhey, R.F., *Complex Variables and Applications*, McGraw-Hill, Fourth Edition (1990).
9. Kreyszig, E., *Advanced Engineering Mathematics*, John Wiley & Sons, Sixth Edition (1988).
10. Zhu, Z.Q. and Howe, D. "Instantaneous magnetic field distribution in brushless permanent magnet DC motors, part III: Effect of stator slotting", *IEEE Transactions on Magnetics*, **29**(1), pp 143-151 (Jan. 1993).
11. Lee, J.H., Kim, D.H. and Park, Il.H. "Minimization of higher back-EMF harmonics in permanent-magnet motor using shape design sensitivity with B-spline parameterization", *IEEE Transactions on Magnetics*, **39**(3), pp 1269-1272 (May 2003).
12. Zhu, Z.Q., Howe, D., Bolte, E. and Ackermann, B. "Instantaneous magnetic field distribution in brushless permanent magnet DC motors, part I: Open-circuit field", *IEEE Transactions on Magnetics*, **29**(1), pp 124-135 (January 1993).
13. Zhu, Z.Q. and Howe, D. "Instantaneous magnetic field distribution in brushless permanent magnet DC motors, part VI: Magnetic field on load", *IEEE Transactions on Magnetics*, **29**(1), pp 152-158 (Jan. 1993).

APPENDIX 1

Conformal Mapping

By writing f as follows:

$$f(z) = \log(z) = \frac{1}{2}\ln(x^2 + y^2) + j \arctan\left(\frac{y}{x}\right). \quad \text{(A1)}$$

The transformation, $w = \log(z)$, maps the right half plane, $x > 0$, onto the horizontal strip, I, i.e.,

$$I: \quad \pi/2 < v < \pi/2. \quad \text{(A2)}$$

Theorem 1

A function, $f(z) = u(x, y) + jv(x, y)$, is analytic in a domain, D, if, and only if, v is a harmonic conjugate of u, i.e.,

$$u_{xx}(x, y) + u_{yy}(x, y) = 0,$$

$$v_{xx}(x, y) + v_{yy}(x, y) = 0. \; \dagger \quad \text{(A3)}$$

It can easily be shown that the component functions, u and v, of $\log(z)$, Equation A1, satisfy the partial differential Equations A3. So, this function is analytic on D.

Definition 1

The transformation, $w = f(z)$, is called a conformal mapping at z_0 if the value (magnitude) and direction (sense) of the angle of inclination of any two smooth arcs, C_1 and C_2, passing through z_0, are preserved. †

Theorem 2

The mapping, $w = f(z)$, is conformal in D if f is analytic in D and its derivative, $f'_{(z)}$, has no zeros there. †

Using Theorem 2 and Definition 1, it can be shown that transformation, $w = f(z) = \log(z)$, is a conformal mapping [8,9].

APPENDIX 2

Brushless PM Motor Parameters

Magnet arc angle ($2\alpha_m$)	65 mechanical degrees
Magnet material	Nd-Fe-B, N33
Relative recoil permeabilit (μ_r)	1.05
Remanence (B_{res})	1.1 Tesla
Rotor lamination material	M19,26 Gage
Stator lamination material	M36,26 Gage
Stator outer radius (r_{so})	97.1 mm
Stator slot opening (b_o)	5.1 mm
Stator tooth depth (h_t)	17.2 mm
Stator yoke depth (h_y)	17.4 mm

APPENDIX 3

Back-EMF Calculations

The current and back-EMF are supposed as follows. The flux linking a stator coil is calculated from [12,13]:

$$\psi = \sum_n \frac{\Phi_n}{np} K_{yn} \cos(np\alpha), \tag{A4}$$

where Φ_n and K_{yn} are defined in [12,13]. Therefore, the EMF induced at each turn of a coil is:

$$e_{1\ \text{turn}}(t) = \frac{d\psi}{dt}, \tag{A5}$$

and the induced EMF at each phase is obtained as:

$$e_{\text{phase}}(t) = \sum_n \omega_r \Phi_n K_{yn} K_{wn} N_S \sin(np\alpha), \tag{A6}$$

where N_s is the number of turns per phase and $K_{wn}(= K_{d,n} * K_{p,n} * K_{skew,n})$ is the nth harmonic of the winding factor.